Applied Clay Science 262 (2024) 107587

Contents lists available at ScienceDirect

Applied Clay Science

journal homepage: www.elsevier.com/locate/clay

Research Paper

Effects of different China and ball clays on traditional ceramic process: A multi-methodological approach

Andrea Bernasconi [a,*], Nicoletta Marinoni [b], Lucia Mancini [c], Marco Voltolini [b], Fernando Francescon [d], Rinaldo Sartori [d], Alessandro Pavese [a]

[a] Dipartimento di Scienze della Terra, Università di Torino, Via Valperga Caluso 35, 10125 Torino, Italy
[b] Dipartimento di Scienze della Terra "Ardito Desio", Università degli Studi di Milano, Via Botticelli 23, 20133 Milano, Italy
[c] Department of Materials, Slovenian National Building and Civil Engineering Institute (ZAG), Dimičeva ulica 12, 1000 Ljubljana, Slovenia
[d] Ceramica Dolomite S.p.A, Via Cavassico Inferiore, 160, 32026 Borgo Valbelluna, (BL), Italy

ARTICLE INFO

Keywords:
Clay raw materials
Vitreous-China technology
Phase analysis
Ceramic properties
X-ray diffraction
Synchrotron X-ray micro-tomography

ABSTRACT

A combination of technological properties, mineralogical composition and three-dimension (3D) imaging is proposed to get insights into sanitary-ware ceramic bodies of the Vitreous-China technology as a function of the different clay raw materials used in the formulation of slip. Particular attention is paid to the effects induced along the production chain, during casting, after drying (dried body) and after firing (fired body).

The different combinations of China and ball clays lead to different casting behaviour, in first instance, and to different mechanical strength, then, due to variations in the particle size distribution rather than in the mineralogical composition. In particular, the finer the particle size, the finer the pore size and, in addition, the better the mechanical properties (with a maximum of 4.7 MPa), due to a better packing. However, fine particle size distribution worsens the slip's behaviour into moulds, impacting negatively on productivity, with a 17 % reduction of casting thickness.

Upon firing process, such differences are mitigated by the body densification and result in more similar pores' distributions, though the importance of the mineralogical composition is revealed. In fact, differences in mineralogical phases' contents and in kaolinite HI index guide the comprehension of high temperature phase evolution and technological properties like the fired body thermal expansion, foremost via residual quartz.

These results are important for a plastic raw materials's selection within the ceramic sanitary-ware process.

1. Introduction

Whiteware ceramics are defined as fired ceramic bodies (either glazed or unglazed), typically white in colour and fine in texture, designed with proper technical/aesthetical characteristics in light of the target manufacturing industry like, for example, tile, porcelain, sanitary-ware and dinnerware (Carty and Senapati, 1998). Their formulations consist of a mixture of natural raw materials such as clay minerals, fluxing agents and fillers. Clay minerals are known to provide plasticity during the shaping process (typically pressing or slip casting), and mostly consist of kaolinite, illite, and eventually small amounts of smectite/montmorillonite. Fluxing agents, typically feldspar or possibly nepheline syenite, promote the formation of a viscous liquid phase above 1100 °C that progressively fills empty spaces and shrinks the body through a mechanism called "densification". Quartz is widely used as a filler: it generally provides the coarsest particles in the "green body", i.e. the semi-finished product, and contributes to the skeletal network upon firing, thus mitigating shrinkage and deformation of the body.

Several studies have been published about the effects of the mineralogical composition, as well as of the grain size of the filler and flux component, on some technological properties of the ceramic product, although most investigations are focused on the tile/porcelain manufacturing case (Tarvornpanich et al., 2008; Martin-Martinez et al., 2008; Alves et al., 2012).

The ceramic sanitary-ware field has received little attention, hitherto. In this production, a slip is prepared by water-mixing selected raw materials to obtain a suspension with appropriate density and rheological properties, tuning water and/or de-flocculating agent addition (Barnes et al., 1989).

The "green body" must be carefully dried to remove the excess water

* Corresponding author.
E-mail address: andrea.bernasconi@unito.it (A. Bernasconi).

https://doi.org/10.1016/j.clay.2024.107587
Received 11 June 2024; Received in revised form 30 September 2024; Accepted 30 September 2024
Available online 30 October 2024
0169-1317/© 2024 The Authors. Published by Elsevier B.V. This is an open access article under the CC BY license (http://creativecommons.org/licenses/by/4.0/).

before glazing and finally firing. All these steps require a proper matching between technological properties, mineralogical composition and microstructural features, to prevent possible flaws in the final product. This is the case, for example, of the thermal expansion behaviour that can be affected significantly by the raw materials particle size (Bernasconi et al., 2011) or by the densification degree of the body (Bernasconi et al., 2023).

The plastic component of the slip (clays and kaolinite), which in the case of the most diffused sanitary-ware technology known as Vitreous-China (hereafter "VC"; Bernasconi et al., 2011) represents about one half by mass, can differently affect all the ceramic slip characteristics through its mineralogical composition, particle size and morphology (Dondi et al., 2008; Galos, 2011; Ndlovu et al., 2011; Blachier et al., 2014; Kim and Hwang, 2019; Abbasi et al., 2021). About half of the plastic component is represented by "China clay", corresponding to the coarser plastic fraction due to limited or moderate transportation after weathering, which results in full absence or moderate occurrence of accessory minerals such as titanium and iron oxides (Burst, 1991). A China clay might be high-grade or low-grade, depending on the amount of further minerals such as illite and non plastic components (Dondi et al., 2014).

The remaining part of the plastic component is provided by the "ball clays", characterized by more than 50 wt% finer than 2 μm (Bougher, 1995; Dondi et al., 2014), leading to a drying rate reduction and to a larger shrinkage, with the advantage of a better plasticity (Burst, 1991). The finer particle size of ball clays is ascribable to a deep weathering origin, an extensive alteration, in combination with transportation and accumulation. This difference in terms of genetic environments results in a larger kaolinite fraction and higher aluminium content (Wilson, 2008; Manning, 1995), and in a corser particle size distribution in China clays rather than in ball clays.

The mineralogical and chemical composition of clays can also affect the body thermal behaviour, as pointed out by Chin et al. (2017). The occurrence of expandable clay minerals as smectite is known to increase the viscosity of the slurry while the presence of K_2O, generally associated with illite, is important to promote densification and thus reduce the porosity of the fired body (Dondi et al., 2008). Structural order of clay mineral is also important: in the case of kaolinite a lower structural order is in general observed in finer kaolinites, and results in a better sintering behaviour of the fired body (Galos, 2011). The presence of a major kaolinite is at the origin of the shrinking of the body upon heating, because of its dehydroxylation into metakaolinite in the 500–650 °C range. This shrinking effect can be mitigated by the presence of illite and quartz, in particular through the expansivity of the former from room temperature to about 800 °C (Lecomte-Nana et al., 2011) and by the α-quartz linear thermal expansion from room temperature to about 573 °C (Carpenter et al., 1998; Johnson et al., 2021). In general, both China and ball clays mineralogical composition can vary a lot, both in terms of present phases and in terms of relative quantities, as pointed out by several authors (Dondi et al., 2008; Kim and Hwang, 2019).

Despite all these effects, a rationalization of the relationship between clays, resulting slip's manifold features and ceramic body's properties is still little known, and much of the current comprehension relies upon barely heuristic trial-and-error approaches.

In the present paper, sanitary-ware ceramic slips and bodies formulated with different plastic raw materials have been investigated with a multi-methodological approach to shed light on the correlations between clays and intermediate-final products' properties. Such an aspect is crucial for designing a strategy to choose the plastic component so as to maximize the quality and efficiency of the wholesale production. This study features, for the first time to our knowledge, a combination of complementary techniques like X-ray powder diffraction (XRD) and synchrotron X-ray computed micro-tomography (*SR* μCT), with technological properties measured along the manufacturing chain. XRD discloses the different minerals involved in the raw materials and their relative abundances, as well as the after firing residual and new formation phases, glass included. *SR μCT* enables to image the internal structure of a ceramic sample, investigating morphological features and the topology of voids through a non-destructive method and in a the three-dimensional (3D) domain (Marinoni et al., 2012; Caruso et al., 2020; Kudrna et al., 2018; Possenti et al., 2019).

2. Materials and methods

2.1. Raw materials

A number of commercial raw materials with characteristics suitable for the sanitary-ware production have been selected. In particular, special attention has been paid to the plastic component, with the selection of two China clays (*CC1* and *CC2*) and two ball clays (*BC1* and *BC2*), in light of their different particle size distribution, chemical and phase composition. Quartz, feldspar and VC-pitcher (i.e. fired ceramic scraps from VC production) have been also introduced in the formulation of slip. Raw materials' chemical compositions are summarized in Table 1.

2.2. Slip preparation

Three VC slip formulations were prepared by varying the plastic composition and preserving the amounts of quartz, feldspar and VC-pitcher, according to Table 2, so that the effects on the "green body" and final ceramics are attributable to clays only. The chemical compositions of the three slip samples are summarized in Table 3. In light of the different particle size distribution, chemical and phase composition of the plastic component, the slips here under investigation represent three "extreme" formulations that are compatible with the wholesale production, and for this reason of particular interest.

Each slip was prepared to mimic common industrial conditions. Every mixture was stirred for 20 min, with a slurry density of about 1860 g/l. After an aging time of 24 h, a final adjustment of the slip density was performed (values are summarized in Table 2) and ~ 0.4 wt % sodium silicate deflocculant (dried base) was added, to reproduce rheological conditions similar to those of the wholesale production. A Gallenkamp-type torsional viscosimeter was used to measure the viscosity immediately after stirring the slip at 500 rpm. Note, in Table 2, that the higher the measured torsion of the viscosimeter in degrees (*V0'*), the lower the slip viscosity. We refer to such a kind of sample as "slip" or "*slurry*" (slip is used in a very general fashion to address a water suspension with raw materials; *slurry* is strictly associated with slip at the conditions reported above).

Finally, each slip was cast into cylinders with length and diameter respectively of 8 and 1 cm. After 1 h, the cylinders were demoulded, left in atmosphere for 12 h to avoid the formation of cracking upon drying, and finally dried at 105 °C for 24 h. For each slip composition, 8 cylinders were cast, for characterization before firing; we call this kind of sample "*dried body*".

Additional 8 cylinders were cast for characterization of the fired bodies. Such samples were heated in an electric kiln at a maximum temperature of 1200 °C using a heating/cooling rate of 5 °C/min and a plateau at a maximum temperature of 5 min. We refer to this kind of sample as "*fired body*".

2.3. Particle size distribution analysis

In the case of both China clays and ball clays, the particle size distribution analysis was performed using a Sedigraph 5100, which relies on the speed of water dispersed particles following the Stoke's law. The particle size distribution of slip is coarser than those of China clays and ball clays alone; for this reason, it was measured using a Malvern Mastersizer 3000, which is based on laser diffraction of water dispersed particles. More details about sample preparation for both types of measurement are available in Section A.1.

Table 1
Raw materials chemical composition in weight percentage from XRF analysis. Average uncertainty ±1 %.

Raw material	SiO_2	Al_2O_3	Fe_2O_3	TiO_2	CaO	MgO	K_2O	Na_2O	Loss on Ignition
CC1	47.72	36.79	0.95	0.05	0.07	0.30	1.99	0.10	12.03
CC2	48.13	36.27	0.90	0.06	0.04	0.40	2.59	0.06	11.56
BC1	53.30	30.90	1.04	1.06	0.20	0.28	1.90	0.20	10.90
BC2	51.98	30.87	1.20	0.98	0.20	0.28	1.89	0.20	12.40
Quartz	99.37	0.40	0.04	0.01	0.02	0.01	0.05	0.05	0.05
Feldspar	68.30	18.80	0.23	0.19	2.30	0.27	0.21	9.20	0.50
VC-pitcher	69.49	23.61	0.61	0.40	0.70	0.28	1.82	2.95	0.15

Table 2
Slip composition (wt%), density (g/l) and rheological reference property (deg).

Sample	*VC1*	*VC2*	*VC3*
CC1	30	0	30
CC2	0	30	0
BC1	24	24	0
BC2	0	0	24
Feldspar	21	21	21
Quartz	19	19	19
VC-pitcher	6	6	6
Density (g/l)	1855	1854	1851
V0' (deg)	290	320	292

2.4. Casting thickness attitude

The "casting thickness attitude" of each *slurry* was determined by 30 min filtering in a Baroid stainless steel filter press cell at 5 bar of pressure and 5 min draining the excess solution. The "wet weight" (b_w) of the resulting "cake" was measured by an analytical balance; then, the "dry weight" (b_d) was determined by weighting after drying in an oven for 24 h at 110 °C. The "cake" moisture (mo) was calculated by the following equation:

$$mo = \frac{b_w - b_d}{b_d} \times 100 \quad (1)$$

This measurement was repeated five times for each slip formulation, to check the full reproducibility of the results and estimate statistical oscillations.

2.5. Mercury intrusion porosimetry (MIP)

Mercury Intrusion Porosimetry (MIP) was employed to investigate the accessible porosity of the *dried body*. The measurements were carried out with a Thermo Scientific mercury intrusion porosimeter Pascal 140 + Pascal 240. MIP data were collected in the pore radius range 50–0.0037 μm (pressure: 0.02–200 MPa), which encompasses from meso- to mega-pores according to the IUPAC classification (Rouquerol et al., 1994; Sing, 1995). The volume resolution is 0.1 mm^3 and accuracy is >0.2 %. MIP results have been expressed as bulk density, corresponding to the mass of dried slip per unit volume, and in terms of average, modal and median values of the pore size distribution.

2.6. Mechanical properties

The Modulus of Rupture (MoR) was determined on both *dried body* and *fired body* by using an Alpha technologies T2000-tensiometer working with 3-points bend condition to get the strain-stress curve of the sample. MoR was determined as:

$$MoR = \frac{|(3 \times F_b) \times L_S|}{(2 \times b \times S^2)} \quad (2)$$

where F_b and L_s are the three points flexural breaking load (force) and the distance between the tension rods on which a sample bar is laid, respectively. b and S correspond to breadth and thickness of the bar, respectively. Eight bars of each slip formulation were measured.

2.7. Water absorption

For each *fired body* sample, the water absorption (WA) was measured on test bars of 8 cm, after mechanical test. The protocol consists in drying a bar for 12 h at 110 °C and weighing it by an analytical balance to determine the dry weight (w_d). Afterward, the bar is boiled in water for 2 h, cooled to room temperature in the same water and finally weighed to get the wet weight (w_w). The WA value was calculated as reported beneath:

$$WA = \frac{w_w - w_d}{w_d} \times 100 \quad (3)$$

This measurement was performed five times, for each slip formulation.

2.8. Dilatometric test

For each slip composition, a *fired body* specimen 50 × 5 × 5 mm^3 in size was cut from a fired cylinder and thermal dilation measurements were carried out using a Netsch Dilatometer 402ED in the 20–650 °C temperature range, with a heating ramp rate of 10 °C/min. The linear thermal expansion coefficient (α) was determined as:

$$L = L_0 e^{[\alpha(T - T_0)]} \quad (4)$$

where L and L_0 represent the specimen's length at temperature T and T_0, respectively, the latter corresponding to the room temperature. This measurement was performed five times, for each slip formulation.

2.9. X-ray powder diffraction (XRPD)

XRPD data were collected using a θ-2θ Bragg-Brentano para-focusing PANalytical X' Pert PRO diffractometer (Cu Kα radiation) equipped with a multichannel X' Celerator detector. Samples were ground, mounted in aluminium sample holders using the side-loading techniques and diffraction signals were recorded in the 5–80° 2θ range.

XRPD patterns were processed by Rietveld method using the GSAS-II package (Toby and Von Dreele, 2013). In the case of *fired body* samples,

Table 3
Slip chemical composition in oxides (wt%), obtained by combination of data in Tables 1 and 2. Average uncertainty of ±1 %, estimated by error propagation.

Slip	SiO_2	Al_2O_3	Fe_2O_3	TiO_2	CaO	MgO	K_2O	Na_2O	Loss on Ignition
VC1	65.18	23.52	0.62	0.33	0.55	0.23	1.21	2.01	6.34
VC2	65.30	23.37	0.61	0.33	0.54	0.26	1.39	2.00	6.20
VC3	64.81	23.52	0.66	0.31	0.55	0.23	1.21	2.01	6.20

10 wt% corundum NIST 676a (Cline et al., 2011) was added as internal standard to estimate the amorphous content, X_{glass}, by the equation:

$$X_{glass} = 1 - \frac{X_{Al_2O_3}}{X_S} \times \left(\frac{1}{X'_{Al_2O_3}} - 1 \right) \quad (5)$$

where $X_{Al_2O_3}$, X_s and $X'_{Al_2O_3}$represent the weight fraction of corundum NIST 676a, the weight fraction of sample and the Rietveld refined fraction of corundum NIST 676a, respectively. More details about the Rieveld refinement data analysis are available in Section A.2.

The crystallinity of kaolinite was determined by means of Hinckley index (HI) (Aparicio and Galan, 1999) as:

$$HI = \frac{A + B}{At} \quad (6)$$

where *A* and *B* are the intensities of the (*1*−*10*) and (−*1*−*11*) peaks after background subtraction, respectively, while *At* is the intensity of the kaolinite (*1*–*10*) peak without background subtraction.

2.10. Synchrotron X-ray computed microtomography (SR μCT)

3D X-ray imaging experiments were performed at the SYRMEP beamline of the third generation synchrotron laboratory Elettra located in Trieste, Italy (Tromba et al., 2010). Measurements were carried out with the samples (both *dried body* and *fired body*) placed on a high-resolution rotation stage and illuminated with a monochromatic beam (energy = 27 keV). For each tomographic scan, 1440 radiographs (projections) of the sample were acquired for equally spaced rotation angles and exposure time of 1 s over a total rotation of 180°. The projections were recorded with a 12-bit water-cooled CCD camera (4008 × 2672 px^2, 4.5 μm × 4.5 μm effective pixel size). In our experiments, the pixel size has been set to 9.0 μm (2 × 2 binning), thus yielding a field of view of 18 mm × 12 mm. To optimize the phase-contrast effects, the sample-to-detector distance was set to 300 mm.

The 3D processing and analysis of the reconstructed images were performed using the *Pore3D* software library developed at Elettra (Brun et al., 2010). The anisotropy of the pores network was quantified by the "Isotropic Index" (hereafter "*I*") as well as by the "Elongation Index" (hereafter "*E*"), which provides a measure of the similarity of a fabric to a uniform distribution. In the case of *I*, its value tends to zero when all the objects are confined to a single plane or axis while it tends to 1 in the case of perfect isotropy. In the case of *E*, its value tends to zero when all the objects are isotropic while it tends to 1 in the case of objects elongated in a unique direction. Finally, pores network and connectivity have been assessed using the "Connectivity Density" index (hereafter "*CD*"), a scalar representing the number of redundant connections normalized to the analyzed volume. Highly-connected networks are characterized by a positive *CD* value whereas negative or close to zero figures are typical of scarcely-connected networks (Brun et al., 2010; Zandomeneghi et al., 2010). Objects below eight voxels size were not considered for morphometric analysis, corresponding to 5832 μm^3.

More details about *SR* μCT image reconstruction are available in Section A.3.

2.10.1. MIP versus SR μCT techniques comparison

MIP and *SR μCT* represent two complementary approaches rather than two equivalent techniques.

MIP relies on the throat size of a connected pore network and it can measure throat size of large range of sizes, in a relative large volume of sample. In the case of *SR* μCT measurements, the measurable range of pore/thoroat sizes becomes significantly smaller in comparison, given the resolution versus sample size problem of the approach, although many other pore network's characteristics becomes accessibile (Voltolini et al., 2017). Therefore, for those samples where nano- and micro-sized pores are present, the direct overlap of the two approaches decreases while the complementarity between MIP and *SR μCT* enhances.

Increasing the resolution of the *SR μCT* measurement to make this technique more comparative than complementary respect MIP would require a much smaller volume to be measured, making the analysis less statistically significant. For this reason, the resolution value of *SR μCT* measurements was chosen to optimize the topological/morphometric analysis (i.e. morphology and connectivity of pores) while MIP provides complementary information about the below-resolution porosity missed by *SR μCT* technique.

2.11. ANOVA analysis

Analysis of variance (ANOVA) was performed in the case of casting thickness attitude, MoR, WA and thermal expansion, to better compare the results from different populations with each other (in our case sample *VC1*, *VC2* and *VC3*) and determine whether they share the same statistical distribution or not (Stahle and Wold, 1989). For each observable, inter-group deviance (SSA), intra-group deviance (SSW), inter-group variance (MSA) and intra-group variance (MSW) were determined. Then, the related Fisher variable (F) was calculated and compared with the critical F-value (F_crit), at a confidence level of 95 % [P (F ≤ F_crit) = 0.95]. In the eventuality of a F larger than a F_crit, the null hypothesis (e.g. there is no difference between populations) is neglected.

The standard deviations of each observable are mentioned in the dedicated table caption.

3. Results and discussion

3.1. Raw materials

The quantitative phase compositions of the two China clays, *CC1* and *CC2*, are reported in Table 4. The two samples have similar mineralogical and chemical compositions: they both bear relevant amounts of kaolinite, foremost, and of illite, in association with very modest quartz contents (about 1 wt%). *CC1* is richer in kaolinite than *CC2*, which has a larger content of illite. The results of the mineralogical phase quantification agree with the chemical composition of Table 1, where the larger K_2O content in *CC2* than in *CC1* is ascribed to a larger amount of illite. The diffraction pattern of *CC1* and the theoretical profile of the Rietveld fitting are shown in Fig. 1a, by way of example.

HI-figures of 1.15 and 1.36 have been found for *CC1* and *CC2*, respectively, and suggest a good degree of crystallinity (higher in *CC2* than in *CC1*), in view of that a value of 0.5 points to poorly crystalline and 1.5 to highly crystalline kaolinite (Aparicio and Galan, 1999). Furthermore, *CC1*, which is characterized by a finer particle size distribution than *CC2*, as shown in Fig. 2a, exhibits a lower degree of crystallinity, in keeping with Galos (2011). According to Dondi et al. (2014), both China clays are classified as from "Low grade" (LH) to "High grade" (HK) kaolinite (Fig. 3).

The quantitative phase compositions of the two ball clays, *BC1* and *BC2*, are reported in Table 4. In comparison with China clays, they exhibit a smaller abundance of kaolinite and a larger content of quartz, in combination with relevant and similar illite amounts (~29 wt%). In the case of ball clays, the results of the quantitative phase analysis are corroborated by the chemical composition of Table 1, where the SiO_2 values are coherent with the amounts in quartz and kaolinite, with respect to China clays. HI ranges between 0.5 and 0.65, as reported in Table 4.

The particle size distribution is fine-grained, with the fraction smaller than 2 μm higher than 50 % by weight (Fig. 2b). More precisely, *BC1*, which is characterized by a finer particle size distribution than *BC2*, exhibits a lower degree of crystallinity, in keeping with Galos (2011). According to Dondi et al. (2014), both clays fall in the ball clays (BC) region, as displayed in Fig. 3.

Table 4
Raw materials quantitative phase analysis. Average uncertainty ±1 % for glass, ±1 % for kaolinite and illite, ±0.5 % for albite, quartz and mullite, ±0.1 % for zircon. HI is displayed for China clays and ball clays. The phases that have been checked in the Rietveld refinements but whose abundance resulted <0.5 wt% in a raw material are characterized by the acronym "np", i.e. not present.

Raw material	Kaolinite	Illite	Plagioclase	Quartz	Mullite	Glass	Zircon	HI
CC1	76.6	22.1	np	1.2	np	np	np	1.15
CC2	71.2	28.0	np	0.8	np	np	np	1.36
BC1	56.9	28.8	np	14.3	np	np	np	0.54
BC2	60.1	29.2	np	10.7	np	np	np	0.63
Feldspar	np	np	85.0	15.0	np	np	np	–
Quartz	np	np	np	100.0	np	np	np	–
VC-pitcher	np	np	np	18.5	20.0	61.3	0.2	–

No evidences of mineralogical phases like feldspar, smectite, halloysite in CC1, CC2, BC1 and BC2 clays have been observed, differently from other cases of study reported in literature (Dondi et al., 2008; Kim and Hwang, 2019). Interestingly, although the chemical analyses data from Table 1 are similar for all four clay samples, important differences in terms of mineralogical composition and HI index have been disclosed.

Finally, the results of the slip hard component raw materials (i.e. quartz, feldspar and VC-pitcher) are reported in Table 4. Feldspar mainly occurs as albite (85 wt%), accompanied by quartz (~15 wt%). Quartz raw material is pure, and other crystalline phases have not been observed within the instrument detection limit (0.1–1 wt% range). VC-pitcher is constituted mostly by a glass phase (~61 wt%), with the occurrence of ~20 and ~ 18.5 wt% of mullite and quartz, respectively.

3.2. Slip and unfired body

The *slurries* and the *dried bodies* of the three slips under investigation reflect the chemical and mineralogical differences of the starting raw materials used in their formulation, as shown in Table 3 and Table 5, respectively.

The highest amount of kaolinite occurs in *VC3*, whereas the lowest one is observed in *VC2*. In general, the differences in kaolinite content between the three slip compositions are around 3 wt% (i.e. 37.3–34.1 wt %). Similar differences are also observed in terms of illite content (i.e. 15.3–13.5 wt%), with the lowest values in the case of *VC1* and *VC3* slips. Quartz achieves its maximum content in *VC1* and *VC2* (i.e. 29.5 wt%). The sum of albite, mullite, glass and zircon is constant, being the content of feldspar and VC-pitcher fixed in the three slips, and it amounts to 21.0 wt%.

As far as the particle size distribution is concerned, differences between the three slips are displayed in Fig. 4, where *VC1* is the most abundant in the range 0–10 μm, whereas *VC3* exhibits the largest figures in the range 10–125 μm. *VC2* and *VC1* are quite similar in the 10–125 μm interval (see Table A.2 for more detailed results).

Table 6 shows the relevant technological properties of the *slurries* and *dried bodies*. The best casting attitude behaviour is shown by *VC2 slurry*, with a wet cake of 94.2 g, slightly higher than *VC3 slurry* (i.e. 93 g), whereas *VC1 slurry* yields the lowest figure (i.e. 78.3 g).

VC1 dried body has a much higher bulk density than *VC2* and *VC3*, with pores significantly smaller than in *VC2* and *VC3*, as shown by average, modal and median values of the pore size distribution.

The mechanical behaviour of the *dried body* displays a minimum MoR value of 3.60 MPa for *VC2* and a maximum figure of 4.74 MPa, in the case of *VC1*.

ANOVA indicates statistically significant differences between *VC1*, *VC2* and *VC3 slurries* for casting thickness, MIP and MoR values.

The results of the *SR* μCT analysis on *dried body* samples are summarized in Table 7. Pores larger than 100 μm are not observed in the three *dried bodies,* and their volume fraction above the instrumental resolution are below 0.1 % in all three samples. These *SR* μCT values are smaller than those observed by MIP approach and they agree with the complementarity between these two techniques in the case of nano- and micro-sized pores, as defined in Section 2.10.1.

E index values close to 0 are shared by all the samples while *I* index shows more scattered values, with *VC2* and *VC1* having pores that exhibit minimum and maximum "sphericity", respectively. Eventually, the values of the *CD* index reflect important differences; in fact, *VC1* is characterized by a figure of 500, to be compared with 70 and 105 for *VC2* and *VC3*, respectively.

Pore size distribution has been also measured by *SR μCT*. The results disclose that *VC3* is characterized by pores of larger size than *VC1* and *VC2* (see Fig. 5a). An example of a virtual section and volume rendering of voids in the case of *dried body* is provided by Fig. 6a.

The results mentioned above suggest that *VC1* has the most packed structure. In fact, *VC1* exhibits the highest bulk density value, as well as the lowest average, median and modal figures of the pore size distribution. Pore size, in turn, could be related to the finest particle size distribution in the 0–10 μm range used for *VC1*, compared with the other two slips. This is associable with the most performant mechanical properties shown by the *VC1 dried body* (i.e. 4.74 MPa of MoR value), among the investigated samples. On the other side, the more packed are the particles of a *dried body*, the smaller is its permeability. Therefore, given that slip casting is governed by permeability through a porous medium (e.g. plaster mould), the baroid cake of *VC1* exhibiting the lowest figure is a coherent finding. Such results agree with those by *SR* μCT. In particular, *CD* index values reach their maximum (i.e. 500) for *VC1*, thus indicating a modest pore connection with respect to the other two *dried bodies*. Moreover, *VC1* has pores of "more spherical" shapes than those of *VC2* and *VC3*, as corroborated by its larger *I* index.

Although the rheological properties commonly have an important role in affecting the characteristics of the green body (Fortuna, 2011) with highly packed particles (deflocculated slip), this does not occur for our *slurries*. In fact, if one looks at the Gallenkamp results of Table 2, the *V0*' values indicate that *VC1* has larger viscosity than *VC2* and *VC3*. Therefore, the rheological properties seem to affect the packing degree of the *VC1 dried body* in a way other than the one expected.

VC2 displays the best performances in terms of casting thickness. This is explained by its coarser particle size distribution of *VC2* with respect to *VC1*, in the 0–10, and *VC3*, in the 10–125 μm range. A coarser particle size distribution typically leads to a less particle-packed cake in the casting thickness attitude tests, thus promoting the permeability of the cake. This feature is in agreement with the modest packing network of *VC2*, as corroborated by its low bulk density (~1.75 g/cm^3). Such high porosity affects the mechanical properties of the *dried body*, as proven by that *VC2* displays the lowest MoR value (i.e. 3.60 MPa), among our slips.

VC3 is characterized by the lowest bulk density value (~1.72 g/cm^3) and by the coarsest pore size profile, as both MIP and *SR μCT* results indicate. Although the mechanical properties of *VC3* are in keeping with some wholesale production values (in the 3.5–5.0 MPa range from our experience), *VC1* yields better performances. Though a less particle-packed body is reasonably associated with a good casting behaviour, this is not expected for mechanical properties, that should worsen. A possible explanation of the better MoR value of *VC3* compared to *VC2* might be related to the lower *E* index and higher *I* index of voids in the former. This hints at a "network of voids" tending to a "more ellipsoidal"

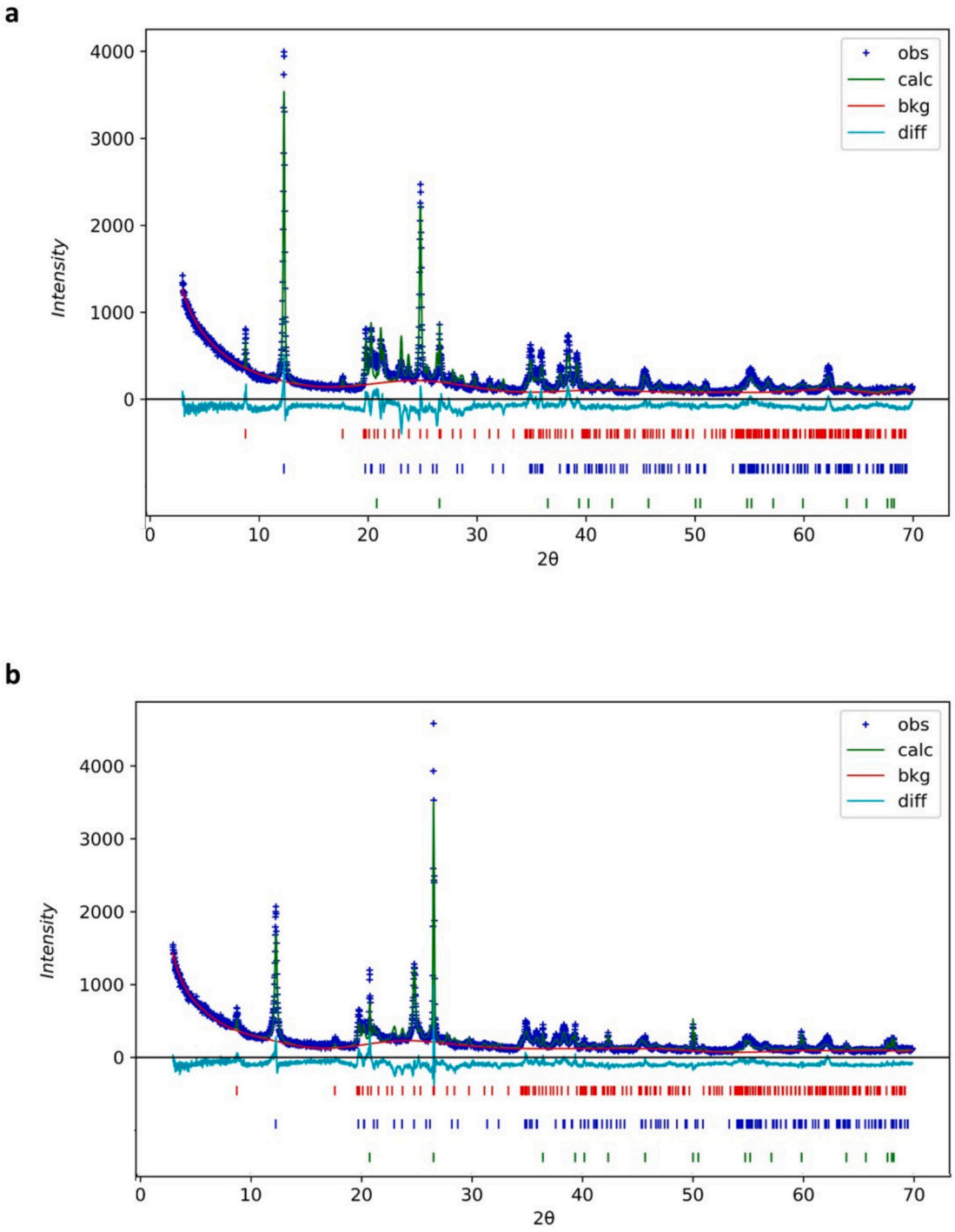

Fig. 1. (a) XRD pattern and Rietveld fit of *CC1* sample and (b) XRD pattern and Rietveld fit of *BC2* sample. The peak positions of the occurring crystalline phases (red: illite; blue: kaolinite; green: quartz) are displayed underneath each pattern. Blue crosses represent the experimental pattern (Obs), green line represents the Rietveld fit, red line represents the background and cyan line represents the difference between the experimental data and the Rietveld fit. (For interpretation of the references to colour in this figure legend, the reader is referred to the web version of this article.)

average shape in *VC2* than in *VC3*. Such a feature has recently been found to underlie the mechanical properties of polymers (Zhu and Majewski, 2020) and advanced ceramics (Das et al., 2024), as in presence of spherical voids almost no stress concentration occurs at the pore surfaces (Rice, 1993).

All these findings suggest that, at the *dried body* stage, the particle size distribution of the plastic component is more important than its mineralogical composition. A simplicistic point of view that merely considers clay minerals (i.e. kaolinite and illite in our system) as responsible of a finer particle size distribution of the slip, and consequently crucial to achieve a better particle packing, would be in error. In fact, although from Table 5 slip *VC3* is clearly richer in clay minerals than *VC1* and *VC2*, the picture emerging from our results is different and well explained by slips' particle size distribution, where the most packed *dried body* is observed in the case of *VC1* slip.

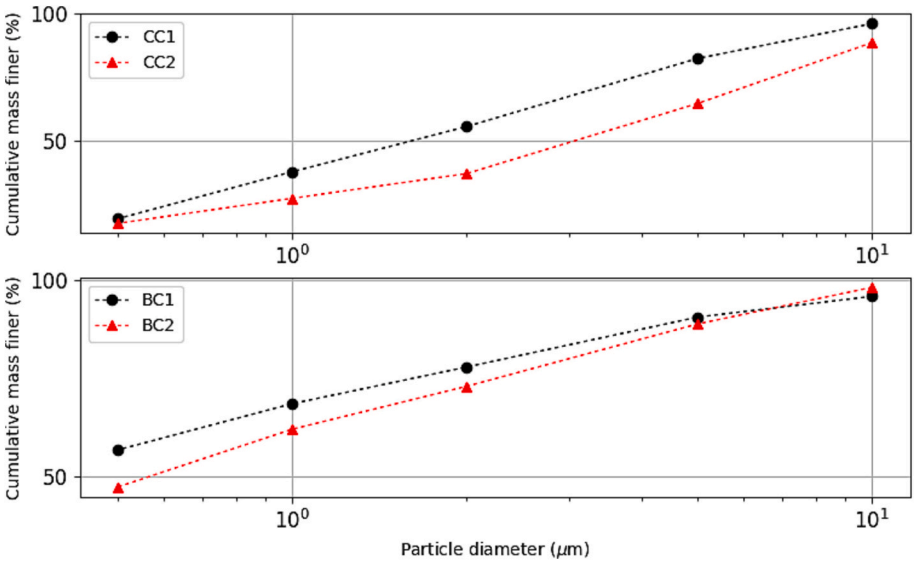

Fig. 2. Sedigraph curves of the China and ball clays under investigation.

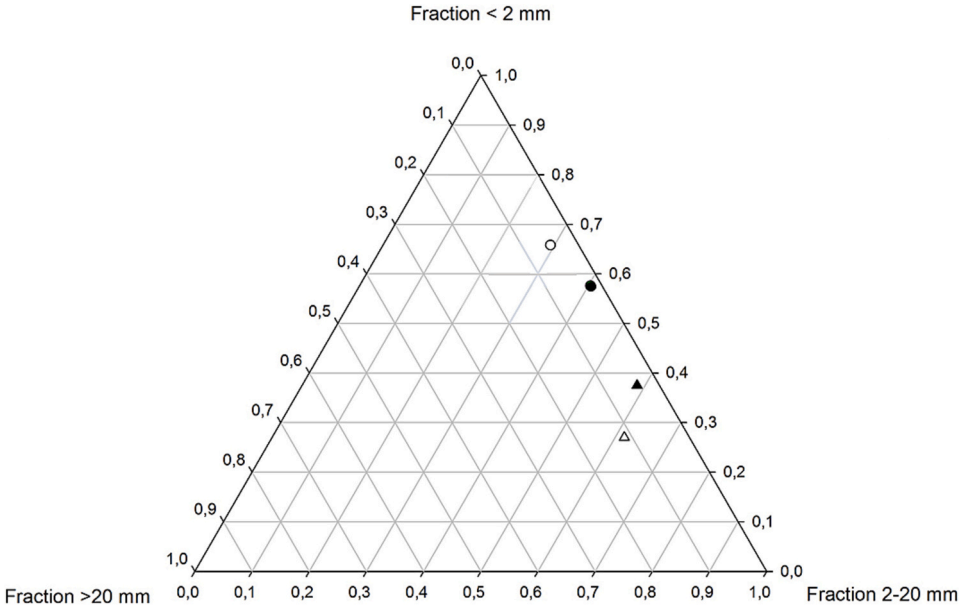

Fig. 3. Plot of the China and ball clays on a ternary particle size charts. White triangle represents *CC1*, black triangle represents *CC2*, white circle represents *BC1* and black circle represents *BC2*.

Table 5
Slip mineralogical composition in wt%. "Others" include mullite, glass and zircon phases.

Slip	Kaolinite	Illite	Albite	Quartz	Others
VC1	35.8	13.5	16.2	29.6	4.9
VC2	34.1	15.3	16.2	29.5	4.9
VC3	37.3	13.6	16.2	28.0	4.9

3.3. Ceramic bodies

In the case of the *fired bodies*, the investigated technological properties are MoR, WA and thermal expansion (see Table 8).

VC2 exhibits the higher MoR values (i.e. 79.8 MPa), whereas *VC1* and *VC3* are characterized by slightly lower and similar figures (i.e. 75.7 and 76.3 MPa, respectively).

All of the samples yield WA values very close to zero, suggesting a complete densification level has been achieved upon firing.

The linear thermal expansion coefficients (α) in the 20–600 °C temperature range are similar to each other (6.81–7.26 10^{-6} 1/°C), though statistically distinguishable, with *VC3* showing the lowest value.

In terms of mineralogical composition, the three investigated ceramic *fired bodies* are characterized by a dominant glass fraction, as hinted by the "bump" in the X-ray diffraction pattern at about 15–30° 2θ (see Fig. 7), in addition to residual quartz and mullite, the latter of new formation. The RIR-Rietveld quantitative phase analysis results are summarized in Table 8. *VC3* has the largest glass content (i.e. 64.2 wt%), whereas *VC2* yields the lowest (i.e. 60.1 wt%). Mullite displays an opposite trend, with *VC2* exhibiting the highest content and *VC3* bearing the lowest. *VC3* is the sample with the lowest content of residual quartz. These results suggest that 60 wt% of glass suffices to provide an appropriate densification degree in the ceramic body, keeping unchanged the firing process parameters, and thereby reach a WA figure

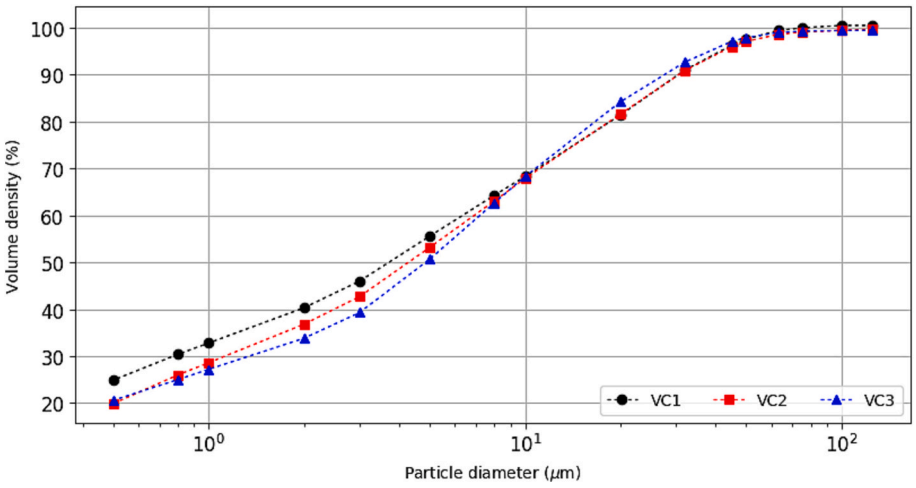

Fig. 4. Laser scattering curves of the three under investigation slips.

Table 6
Results of *dried body* technological properties (casting thickness attitude, MIP and MoR). Average standard deviations are 0.3, 0.3, 0.03, 0.02, 0.003, 0.004, 0.004 and 0.2 for baroid wet, baroid dry, baroid moisture, bulk density, average pore radius, modal pore radius, median pore radius and MoR dry, respectively.

	VC1	*VC2*	*VC3*	P[F ≤ F_crit] = 95 %
Baroid wet (g)	77.6	94.2	93.1	Yes
Baroid dry (g)	64.4	78.3	76.9	Yes
Baroid moisture (%)	20.4	20.3	21.0	Yes
Bulk density (g/cm^3)	1.936	1.751	1.723	Yes
Average pore radius (μm)	0.042	0.057	0.115	Yes
Modal pore radius (μm)	0.093	0.121	0.208	Yes
Median pore radius (μm)	0.064	0.093	0.167	Yes
MoR dry (MPa)	4.74	3.60	4.28	Yes

Table 7
Results of *dried body* analyzed by SR μCT. The volume of interest is 500 × 500 × 500 voxels, corresponding to about 0.20 mm^3.

	VC1	*VC2*	*VC3*
Connectivity density (*CD*) index (mm^{-3})	500	70	105
Elongation (*E*) index	0.022	0.10	0.05
Isotropy (*I*) index	0.83	0.59	0.70

well below the 0.5 % limit of UNI-EN 997. As far as the type of mullite in the three samples, the Rietveld refined unit cell volume of this phase is in the 167.82–167.91 Å^3 range, indicating that 3:2 type is more abundant than 2:1 type, as from neutron diffraction data provided by Murshed et al. (2017).

The ANOVA supports at a confidence level of 95 % the significant difference between *VC1*, *VC2* and *VC3 fired bodies* for MoR, thermal expansion and phase composition.

SR μCT reveals a slightly higher porosity value in the case of VC1 sample (i.e. 3.2 %) compared with *VC2* and *VC3*, whose figures are 2.6 and 2.8 %, respectively (Table 9).

Pore connectivity, expressed by the *CD* index, provides values much larger than in the case of the *dried body*. Similarities between the three *fired body* samples are also observed in the case of both *E* and *I* indexes, thus suggesting that firing induces a densification process leading to a densification that is little affected by the different clays. The pore size distribution shares trends (Fig. 5b) that are close to each other, with a common modal value of 10^{-5} mm^3 and a narrower distribution in the case of *VC3*.

Although the results of the characterization of the *fired body* reveal more similarities between the samples than in the case of the *dried body* (WA is statistically equivalent), some aspects that point out differences emerge, especially as to the mineralogical composition.

For example, the comparison between *VC1* and *VC2* reveals that the coarser and richer in kaolinite China clay used in *VC2* (i.e. *CC2*) than that employed in *VC1* (i.e. *CC1*) led to a lower glass amount in the former, because of the higher upon firing reactivity of the finer raw materials, in keeping with earlier studies from literature (Bernasconi et al., 2011; Bernasconi et al., 2014). If one considers glass content as an indicator of the sintering level of the fired body, our results are in line with the results of Galos (2011), where the author observed a better sintering behaviour in presence of kaolinite with lower degree of crystallinity.

VC3, whose formulation is characterized by the lowest initial content of quartz (Table 5), yields a *fired body* that still displays the smallest residual quartz content, among the samples explored (Table 8). This explains the output of the thermal dilation: the *VC3 fired body* has the lowest α linear thermal expansion coefficient, being less influenced than the other two formulations by the quartz expansivity that is known to boost the metric responsivity to heating of a ceramic body in the range RT-600 °C (Johnson et al., 2021). Thermal expansion behaviour of the body is known to be important in the case of glazed ceramics: it has to be harmonized with thermal expansion behaviour the glaze, with the general rule to have an α of the body larger than the α of the glaze, in order to maintain the glaze under compression and avoid it to craze (Plesingerola and Kovalcikova, 2003; Bernasconi et al., 2023).

Mullite's content, which is recognised as one of the parameters responsible of the mechanical strength of a porcelain body (Carty and Senapati, 1998) together with body's fracture toughness (Hsiung et al., 2013) and size of critical defect (De Noni Junior et al., 2008), occurs in *VC2 fired body* about 2 wt% more abundant than in *VC1-VC3*; this might influence the higher MoR of *VC2*, in comparison with *VC1* and *VC3* (see Table 8). Such larger mullite content can be addressed to the higher initial illite content in *VC2* slip compared with *VC1* and *VC3*, indicating that illite can contribute to mullite formation, according to the studies of Sedmale et al. (2006) and of Magagnin et al. (2014), an effect that appears to be tuned by K_2O availability in the system upon firing (Yamuna et al., 2002).

These findings indicate, in first instance, that the *fired body* properties are minimally influenced by an eventual better particle packing at the *dried body* stage, as shown for example by MoR value of *VC1*, which are not the highest as in the the case of *dried body*. Neither vitrification level and *SR* μCT results are affected by a better *dried body* particle packing. The particle size distribution of the plastic component still plays an important role at this stage, but this is mostly in terms of high temperature reactivity, leading to larger glass amount with a finer

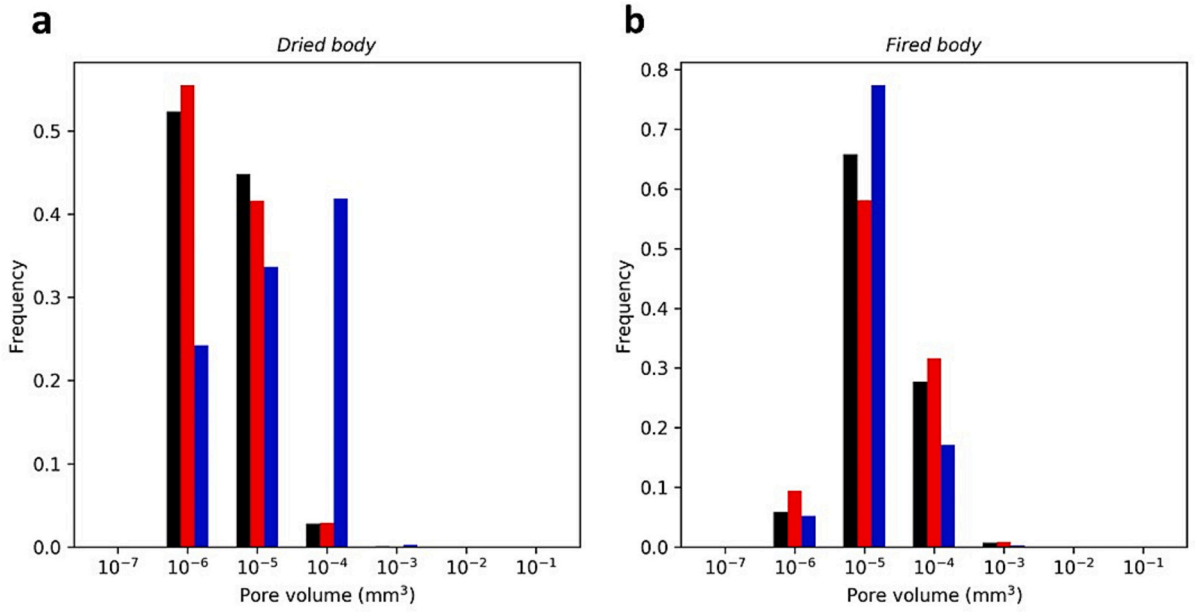

Fig. 5. Pore size distribution obtained by *SR μCT* (a) in the investigated *dried body* samples and (b) in the investigated *fired body* samples. Black bars are referred to VC1 sample, red bars are referred to VC2 sample and blue bars are referred to VC3 sample. (For interpretation of the references to colour in this figure legend, the reader is referred to the web version of this article.)

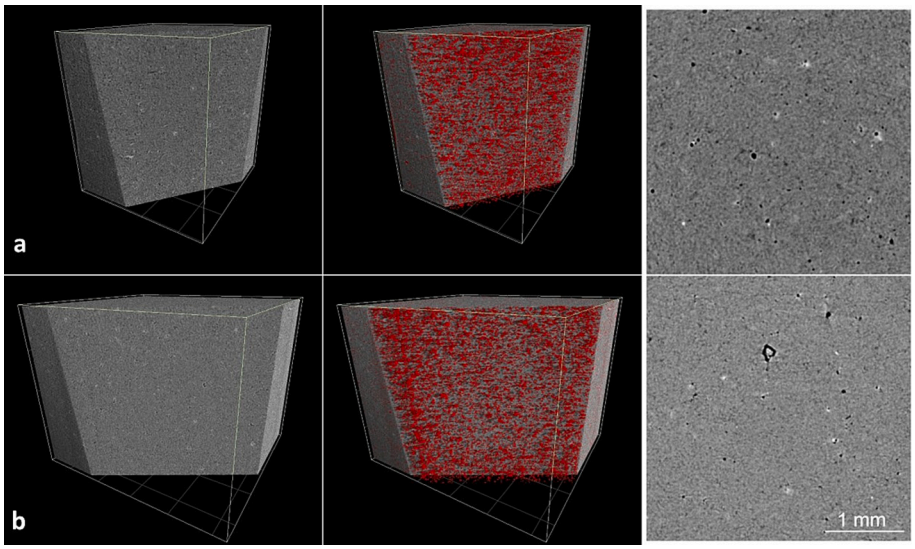

Fig. 6. Images from the SR μCT datasets. (a) the "*VC1 fired body*" sample is featured, showing a volume rendering with a virtual cut, in left right side. In the middle, same volume rendering with the porosity volume highlighted in red superimposed. In the right side a reconstructed slice is shown. (b) the same type of images for the sample "*VC3 fired body*" are shown. (For interpretation of the references to colour in this figure legend, the reader is referred to the web version of this article.)

Table 8
Results of fired body technological properties (Modulus of Rupture, water absorption and thermal expansion) and RIR-Rietveld quantitative phase analysis. Average standard deviations are 10, 0.01, 0.1, 0.3, 0.3 and 0.7 for MoR, Water Absorption, α-quartz, mullite and glass amounts, respectively.

	VC1	*VC2*	*VC3*	P[F ≤ F_0] = 95 %
MoR fired (MPa)	75.7	79.8	76.3	Yes
Water Absorption (%)	0.02	0.01	0.03	Not
α linear thermal expansion coefficient (10^{-6}/°C) 20–600 °C range	7.18	7.26	6.81	Yes
Quartz (wt%)	14.5	15.1	13.8	Yes
Mullite (wt%)	23.0	24.7	22.0	Yes
Glass (wt%)	62.6	60.1	64.2	Yes

particle size distribution. In second instance, these findings indicate that it is the mineralogical composition of the plastic component that appears to be more important in the case of the *fired body*. In fact, larger initial kaolinite amounts appear to increase the total content of glass, as in the case of *VC3*, in keeping with kaolinite-related phase transformation upon temperature which are known to be a source of glass for the fired body. Again, for those slips where the initial quartz content is higher (i.e. *VC1* and *VC2*), the inert nature of such mineralogical phase is disclosed while in the case of *VC3*, the quartz contents is confirmed to be the lowest also at the *fired body* stage, in spite of its coarser particle size distribution.

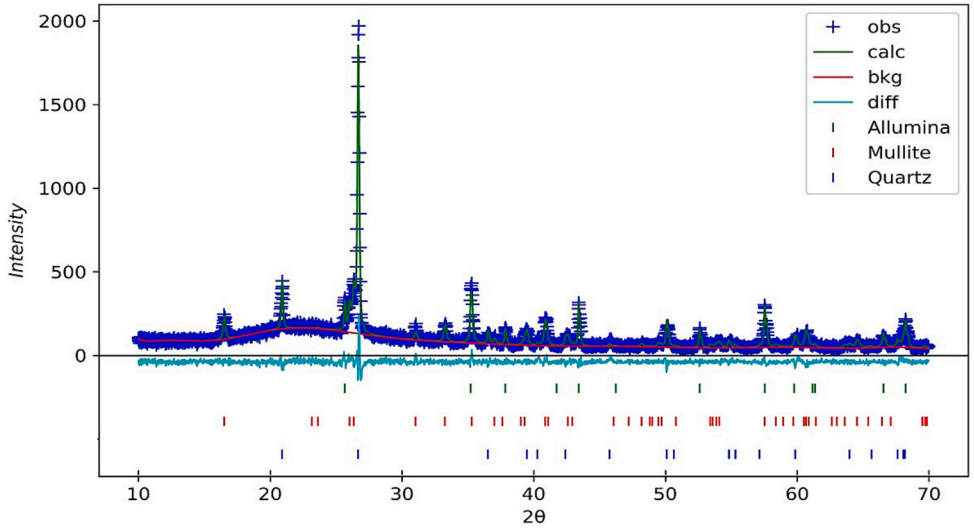

Fig. 7. XRD pattern and Rietveld fit of VC3 *fired body* sample. The peak positions of the occurring crystalline phases (green: quartz; red: mullite; blue: corundum) are displayed underneath the pattern. (For interpretation of the references to colour in this figure legend, the reader is referred to the web version of this article.)

Table 9
Results of *fired body SR μCT*. The volume of interest is 500 × 500 × 500 voxels, corresponding to about 0.20 mm^3.

	VC1	*VC2*	*VC3*
Pore amount (vol%)	3.2	2.6	2.8
Connectivity density (*CD*) index (mm^{-3})	2866	2660	3380
Elongation (*E*) index	0.02	0.04	0.06
Isotropy (*I*) index	0.73	0.69	0.73

4. Conclusions

Vitreous-China sanitary-ware products are affected by the clays used in the slip formulation. Although slip's chemical composition might appear similar, differences in phase composition (i.e. kaolinite, illite and quartz) are present. This study is a contribution to the rationalization of this heuristic observation, employing different clays and a multi-methodological characterization of *dried* and *fired bodies*, which represent the output of two crucial steps of the manufacturing chain. In particular:

1) differences in particle size distribution and mineralogical composition are observed to occur between the investigated types of raw clays used in slip. In particular, ball clays are finer, richer in quartz and poorer in kaolinite than China clays. Moreover, kaolinite in ball clays exhibits a lesser degree of crystallinity than in China clays. Significant differences in particle size distribution and mineralogical compositions are also revealed between the ball clay (*BC1-BC2*), and between the China clay raw materials (*CC1-CC2*);
2) as far as *slurry* and *dried body* are concerned, the particle size distribution of the plastic component appears to be more important than its mineralogical composition. In fact, the finer the particle size of slip, especially in the 0–10 μm range, the higher the resulting bulk density and the lesser the pore connectivity. This leads to an important improvement of the mechanical performances of the material. In the industrial practice, having satisfactory mechanical properties of the *dried body* helps prevent from occurrence of cracking midway the manufacturing chain. Conversely, a slip of fine particle size, especially in the 0–10 μm range, reduces the permeability, thus implying a likely increase of the casting time (~ 17 %) to reach the desired body's thickness, at the expenses of productivity;
3) as for *fired body*, it has been observed that the densification process mitigates the particle packing differences emerging at the *dried body* stage due to plastic component particle size. It is, in particular, the case represented by WA that is the most critical parameter of finite ceramic *VC*-product. At this stage, although a finer particle size of the plastic component is observed to increase the high temperature reactivity, it is the mineralogical composition that appears to be more important. This is supported by differences in the formation of mullite and glass phases, as well as in the residual quartz content, with direct implication on some technological properties.
4) XRD characterization, in terms of HI index for plastic component and in terms of QPA, for both plastic component and fired body, guides the comprehension of technological results while *SR* μCT technique provides complementary information respect MIP, as corroborated by the parameters describing pores' connection and shape.

These results, whose significance level has been assessed by ANOVA, have a role in optimizing the slip formulation. Especially, in those stages that anticipate the firing and are frequently underrated, although they might be an important cause of scraps, in the case of poor mechanical properties, or they might be the reason of a diminution in production, in the case of slow casting rate. Table 10 summarizes the main two guidelines provided by the present study to be considered within the ceramic process.

CRediT authorship contribution statement

Andrea Bernasconi: Writing – original draft, Methodology, Investigation, Formal analysis, Data curation. **Nicoletta Marinoni:** Writing – review & editing, Methodology, Investigation, Data curation. **Lucia**

Table 10
Summary of the effect, reason and process implication emerging from the main clay characteristics observed in the present study.

Clay characteristic	Effect	Reason	Process implication
PSD reduced in the 0–10 μm range	*Dried body* MoR improvement, slip permeability loss	More packed microstructure (smaller pores with limited connectivity)	Dry cracking probability diminution, longer casting time
Lower quartz content	Reduction in the α linear thermal expansion coefficient of *fired body*.	Less residual quartz	α bulk - α glaze delta diminution

Mancini: Writing – review & editing, Investigation. **Marco Voltolini:** Writing – review & editing. **Fernando Francescon:** Writing – review & editing, Conceptualization. **Rinaldo Sartori:** Writing – review & editing. **Alessandro Pavese:** Writing – review & editing, Resources, Conceptualization.

Declaration of competing interest

None.

Data availability

Data will be available on request.

Appendix A. Supplementary data

Supplementary data to this article can be found online at https://doi.org/10.1016/j.clay.2024.107587.

References

Abbasi, Moud A., Poisson, J., Hudson, Z.M., Hatzikiriakos, S.G., 2021. Yield stress and wall slip of kaolinite network. Phys. Fluids 33, 053105. https://doi.org/10.1063/5.0050541.

Alves, H.J., Melchiades, F.G., Boschi, A.O., 2012. Effect of feldspar particle size on the porous microstructure and stain resistance of polished porcelain tiles. J. Eur. Ceram. Soc. 32, 2095–2102. https://doi.org/10.1016/j.jeurceramsoc.2012.03.019.

Aparicio, P., Galan, E., 1999. Mineralogical interference of kaolinite crystallinity index measurements. Clay Clay Miner. 47, 12–27. https://doi.org/10.1346/CCMN.1999.0470102.

Barnes, H.A., Hutton, J.F., Walters, K., 1989. An Introduction to Rheology. Elsevier Science Publisher, Amsterdam, The Netherlands.

Bernasconi, A., Diella, V., Pagani, A., Pavese, A., Francescon, F., Young, K., Stuart, J., Tunnicliffe, L., 2011. The role of firing temperature, firing time and quartz grain size on phase-formation, thermal dilatation and water absorption in sanitary-ware vitreous bodies. J. Eur. Ceram. Soc. 31, 1353–1360. https://doi.org/10.1016/j.jeurceramsoc.2011.02.006.

Bernasconi, A., Marinoni, N., Pavese, A., Francescon, F., Young, K., 2014. Feldspar and firing cycle effects on the evolution of sanitary-ware vitreous body. Ceram. Int. 40, 6389–6398. https://doi.org/10.1016/j.ceramint.2013.11.139.

Bernasconi, A., Bernasconi, D., Francescon, F., Sartori, R., Pavese, A., 2023. Fine Fireclay (FC) body technological properties and mineralogy by tuning slip composition and raw materials particle size distribution. Ceram. Int. 49, 28224–28232. https://doi.org/10.1016/j.ceramint.2023.06.077.

Blachier, C., Jacquet, A., Mosquet, M., Michot, L., Baravian, C., 2014. Impact of clay mineral particle morphology on the rheological properties of dispersions: a combined X-ray scattering, transmission electronic microscopy and flow rheology study. Appl. Clay Sci. 87, 87–96. https://doi.org/10.1016/j.clay.2013.11.004.

Bougher, K., 1995. Ceramic bodyreformulation procedure with emphasis on ball clays. In: Ceramic Engineering and Science Proceedings, pp. 15–20. https://doi.org/10.1002/9780470314708.ch4.

Brun, F., Mancini, L., Kasae, P., Favretto, S., Dreossi, D., Tromba, G., 2010. Pore3D: a software library for quantitative analysis of porous media. Nucl. Instrum. Methods Phys. Res. Sect. An Accel. Spectrom. Detect. Assoc. Equip. 615, 326–332. https://doi.org/10.1016/j.nima.2010.02.063.

Burst, J.F., 1991. The application of clay minerals in ceramics. Appl. Clay Sci. 5, 421–433. https://doi.org/10.1016/0169-1317(91)90016-3.

Carpenter, M.A., Salje, E.K.H., Graeme-Barber, A., Wruck, B., Dove, M.T., Knight, K.S., 1998. Calibrating of excess thermodynamic properties and elastic constant variations associated with the α <−> β phase transition in quartz. Am. Mineral. 83, 2–22. https://doi.org/10.2138/am-1998-1-201.

Carty, W.M., Senapati, U., 1998. Porcelain—raw materials, processing, phase evolution, and mechanical behavior. J. Eur. Ceram. Soc. 81, 3–20. https://doi.org/10.1111/j.1151-2916.1998.tb02290.x.

Caruso, V., Marinoni, N., Diella, V., Berna, F., Cantaluppi, M., Mancini, L., Trombino, L., Cattaneo, C., Pastero, L., Pavese, A., 2020. Bone diagenesis in archaeological and contemporary human remains: an investigation of bone 3D microstructure and minero-chemical assessment. Archaeol. Anthropol. Sci. 12, 162. https://doi.org/10.1007/s12520-020-01090-6.

Chin, C.L., Ahmad, Z.A., Sow, S.S., 2017. Relationship between the thermal behaviour of the clays and their mineralogical and chemical composition: example of Ipoh, Kuala Rompin and Mersing (Malaysia). Appl. Clay Sci. 143, 327–335. https://doi.org/10.1016/j.clay.2017.03.037.

Cline, J.P., Von Dreele, R.B., Winburn, R., Stephens, P.W., Filliben, J.J., 2011. Addressing the amorphous content issue in quantitative phase analysis: the certification of NIST standard reference material 676a. Acta Crystallogr. A67, 357–367. https://doi.org/10.1107/S0108767311014565.

Das, D., Lucio, M.D.S., Kultayeva, S., Kim, Y.W., 2024. Effects of pore size on the flexural strength of porous silicon carbide ceramics. Open Ceram. 17, 100521. https://doi.org/10.1016/j.oceram.2023.100521.

De Noni Junior, A., Hotza, D., Cantavella, Soler V., Sanchez, Vilches E., 2008. Analysis of the development of microscopic residual stresses on quartz particles in porcelain tile. J. Eur. Ceram. Soc. 28, 2629–2637.

Dondi, M., Iglesias, C., Dominguez, E., Guarini, G., Raimondo, M., 2008. The effect of kaolin properties on the behaviour in ceramic processing by a range of kaolins from the Santa Cruz and Chubut Provinces, Patagonia (Argentina). Appl. Clay Sci. 40, 143–158. https://doi.org/10.1016/j.clay.2007.07.003.

Dondi, M., Raimondo, M., Zanelli, C., 2014. Clays and bodies for ceramic tiles: reappraisal and technological classification. Appl. Clay Sci. 96, 91–109. https://doi.org/10.1016/j.clay.2014.01.013.

Fortuna, D., 2011. Sanitary-Ware Casting. SETEC Group.

Galos, K., 2011. Composition and ceramic properties of ball clays for porcelain stoneware tiles manufacture in Poland. Appl. Clay Sci. 51, 74–85. https://doi.org/10.1016/j.clay.2010.11.004.

Hsiung, C.H.H., Pyzik, A.J., De Carlo, F., Xiao, X., Stock, S.R., Faber, K.T., 2013. Microstructure and Mechanical Properties of Acicular Mullite, 33, pp. 503–513. https://doi.org/10.1016/j.jeurceramsoc.2012.09.017.

Johnson, S.E., Song, W.J., Cook, A.C., Vel, S.S., Gerbi, C.C., 2021. The quartz α-β phase transition: does it drive damage and reaction in continental crust? Earth Planet. Sci. Lett. 553, 116622. https://doi.org/10.1016/j.epsl.2020.116622.

Kim, J.Y., Hwang, K.T., 2019. Properties of kaolinite as a raw material for porcelain. J. Korean Ceram. Soc. 56, 566–576. https://doi.org/10.4191/kcers.2019.56.6.05.

Kudrna, Prašek M., Pistone, M., Baker, D.R., Sodini, N., Marinoni, N., Lanzafame, G., Mancini, L., 2018. A compact and flexible induction furnace for in situ X-ray microradiography and computed microtomography at Elettra: design, characterization and first tests. J. Synchrotron Radiat. 25, 1172–1181. https://doi.org/10.1107/s1600577518005970.

Lecomte-Nana, G.L., Bonnet, J.P., Blanchart, P., 2011. Investigation of the sintering mechanism of kaolin-muscovite. Appl. Clay Sci. 51, 445–451. https://doi.org/10.1016/j.clay.2011.01.007.

Magagnin, D., Ferreira dos Santos, C.M., Wanderling, A., Jiusti, J., De Noni Jr, A., 2014. Effect of kaolinite, illite and talc on the processing properties and mullite content of porcelain stoneware tiles. Mater. Sci. Eng. A 618, 533–539. https://doi.org/10.1016/j.msea.2014.09.049.

Manning, D.A.C., 1995. Industrial clays: Kaolin (China clay), ball clay and bentonite. In: Introduction to Industrial Minerals. Springer, Dordrecht. https://doi.org/10.1007/978-94-011-1242-0_3.

Marinoni, N., Voltolini, M., Mancini, L., Cella, F., 2012. Influence of aggregate mineralogy on alkali-silica reaction studied by X-ray powder diffraction and imaging technique. J. Mater. Sci. 47, 2845–2855. https://doi.org/10.1007/s10853-011-6114-3.

Martin-Martinez, J., Ma, Rincon, Romero, M., 2008. Effect of firing temperature on sintering of porcelain stoneware tiles. Ceram. Int. 34, 1867–1873. https://doi.org/10.1016/j.ceramint.2007.06.006.

Murshed, M.M., Sehovic, M., Fischer, M., Senyshyn, A., Schneider, H., Gesing, T.M., 2017. Thermal behavior of mullite between 4 K and 1320 K. J. Am. Ceram. Soc. 100, 5259–5273. https://doi.org/10.1111/jace.15028.

Ndlovu, B., Becker, M., Forbes, E., Deglon, D., Franzidis, J.P., 2011. The influence of phyllosilicate mineralogy on the rheology of mineral slurries. Miner. Eng. 24, 1314–1322. https://doi.org/10.1016/j.mineng.2011.05.008.

Plesingerola, B., Kovalcikova, M., 2003. Influence of the thermal expansion mismatch between body and glaze on the crack density of glazed ceramics, ceramics. Silikaty 47, 100–107.

Possenti, E., Colombo, C., Conti, C., Marinoni, N., Merlini, M., Negrotti, R., Realini, M., Gatta, G.D., 2019. Consolidation of building materials with a phosphate-based treatment: effects on the microstructure and on the 3D pore network. Mater. Charact. 154, 315–332. https://doi.org/10.1016/j.matchar.2019.05.037.

Rice, R.W., 1993. Comparison of stress concentration versus minimum solid area based mechanical property-porosity relations. J. Mater. Sci. 28, 2187–2190. https://doi.org/10.1007/BF00367582.

Rouquerol, J., Avnir, D., Fairbridge, C.W., Everett, D., Haynes, J.M., Pernicione, N., Ramsay, J.D.F., Sing, K.S.W., Unger, K.K., 1994. Recommendations for the characterization of porous solids (Technical Report). Pure Appl. Chem. 66, 1739–1758. https://doi.org/10.1351/pac199466081739.

Sedmale, G., Sperberga, I., Sedmalis, U., Valancius, Z., 2006. Formation of high-temperature crystalline phases in ceramic from illite clay and dolomite. J. Eur. Ceram. Soc. 26, 3351–3355. https://doi.org/10.1016/j.jeurceramsoc.2005.10.012.

Sing, K.W., 1995. Reporting physisorption data for gas/solid systems with special reference to the determination of surface area and porosity (Recommendations 1984). Pure Appl. Chem. 57, 603–619. https://doi.org/10.1351/pac198557040603.

Stahle, L., Wold, S., 1989. Analysis of variance (ANOVA). Chemom. Intell. Lab. Syst. 6 (4), 259–272. https://doi.org/10.1016/0169-7439(89)80095-4.

Tarvornpanich, T., Souza, G.P., Lee, W.E., 2008. Microstructural evolution in clay-based ceramics II: ternary and quaternary mixtures of clay. Flux, and quartz filler. J. Am. Ceram. Soc. 91, 2272–2280. https://doi.org/10.1111/j.1551-2916.2008.02394.x.

Toby, B.H., Von Dreele, R.B., 2013. GSAS-II: the genesis of a modern open-source all purpose crystallography software package. J. Appl. Crystallogr. 46 (2), 544–549. https://doi.org/10.1107/S0021889813003531.

Tromba, T., Longo, R., Abrami, A., Arfelli, F., Astolfo, A., Bregant, P., Brun, F., Casarin, K., Chenda, V., Dreossi, D., Hola, M., Kaiser, J., Mancini, L., Menk, R.H., Quai, E., Quaia, E., Rigon, L., Rokvic, T., Sodini, N., Sanabor, D., Schultke, E., Tonutti, M., Vascotto, A., Zanconati, F., Cova, M., Castelli, E., 2010. The SYRMEP beamline of elettra: clinical mammography and bio-medical applications. AIP Conf. Proc. 1266, 18–23. https://doi.org/10.1063/1.3478190.

Voltolini, M., Kwon, T.H., Ajo-Franklin, J., 2017. Visualization and prediction of supercritical CO_2 distribution in sandstones during drainage: an in situ synchrotron

X-ray micro-computed tomography study. Int. J. Greenhouse Gas Control 66, 230–245. https://doi.org/10.1016/j.ijggc.2017.10.002.
Wilson, I.R., 2008. The constitution, evaluation and ceramic properties of ball clays. Ceramica 44, 287–288. https://doi.org/10.1590/S0366-69131998000400002.
Yamuna, A., Devanarayanan, S., Lalithambika, M., 2002. Phase-pure mullite from kaolinite. J. Am. Ceram. Soc. 85, 1409–1413. https://doi.org/10.1111/j.1151-2916.2002.tb00289.x.
Zandomeneghi, D., Voltolini, M., Mancini, L., Brun, F., Dreossi, D., Polacci, M., 2010. Quantitative analysis of X-ray microtomography images of geomaterials: application to volcanic rocks. Geosphere 6, 793–804. https://doi.org/10.1130/GES00561.1.
Zhu, Z., Majewski, C., 2020. Understanding pore formation and the effect on mechanical properties of high speed sintered polyamide-12 parts: a focus on energy input. Mater. Des. 194, 108937. https://doi.org/10.1016/j.matdes.2020.108937.